



Contents lists available at ScienceDirect

Chemical Geology

journal homepage: [www.elsevier.com/locate/chemgeo](http://www.elsevier.com/locate/chemgeo)

## U-Pb systematics and trace element characteristics in titanite from a high-pressure mafic granulite

Jeffrey H. Marsh<sup>a,b,\*</sup>, Andrew J. Smye<sup>c</sup>

<sup>a</sup> School of Earth and Environmental Sciences, Queens College, City University of New York, 6530 Kissena Blvd., Flushing, NY 11367, USA

<sup>b</sup> Department of Earth & Planetary Sciences, American Museum of Natural History, New York, NY 10024, USA

<sup>c</sup> Department of Geosciences, Pennsylvania State University, 332 Deike Bldg., University Park, PA 16802, USA

### ARTICLE INFO

#### Keywords:

Titanite  
U-Pb systematics  
Trace elements  
Common Pb  
Dissolution-precipitation  
Diffusion

### ABSTRACT

Simultaneous acquisition of U-Pb isotope ratios and trace element abundances across titanite crystals formed in an anatectic, high pressure granulite using LA-ICP-MS split-stream analysis has enabled evaluation of titanite compositional systematics and intracrystalline variability during growth and residence in high-temperature, melt-present environments. Although the titanite studied here have a comparatively low initial Pb ( $Pb_0$ ) component ( $Pb_0/Pb^*$ ), the  $Pb_0$  is highly radiogenic relative to model crustal values, indicating inheritance from U-bearing accessory minerals consumed in the melt/titanite-forming reactions. Additionally, titanite crystals typically exhibit core-rim decreases in  $Pb_0/Pb^*$ , as defined by  $^{204}Pb/^{206}Pb$ , calculated  $^{206}Pb_0/^{206}Pb_T$ , and uncorrected  $^{206}Pb/^{238}U$  spot date profiles. Near the margins this is clearly dominated by local U-enrichment, but in the uniformly low-U interiors outwardly decreasing  $Pb_0/Pb^*$  appears to reflect decreasing  $Pb_0$  concentrations during growth. The positive correlation among  $Pb_0$  and Sr concentrations in crystal interiors over length scales of hundreds of micrometers is consistent with each having experienced similarly small degrees of diffusional relaxation. Given the high crystallization temperatures ( $> 800$  °C) and likely slow cooling rates ( $\sim 5$  °C), our data support slow Pb diffusivity in titanite, even at high temperature conditions, as has been proposed in a number of recent studies.

Along the outer  $\sim 50$ – $100$   $\mu m$ , U, Th, Zr, and REE concentrations are variably elevated relative to the crystal interiors, with profiles taking one of two forms: 1) sharply increasing to highest concentrations inboard from the crystal edge and decreasing again to lower values near the crystal edge, or 2) gradually increasing to highest concentrations nearest the crystal edge. High-contrast BSE imaging shows that the former profiles are associated with  $\sim 1$ – $2$   $\mu m$  wide bright bands surrounding polygonal subgrains that tend to be developed where titanite is (or formerly was) in contact with matrix feldspar (i.e. crystallized melt), and are inferred to represent trace-element-enriched dissolution-precipitation reaction fronts. The latter profiles are associated with diffuse, locally wispy, brightness gradients adjacent to resorbed crystal boundaries, subgrain boundaries, or thicker bright bands formed in contact with matrix hornblende crystals, and are interpreted as regions of enhanced element mobility potentially resulting from the development of local micro-porosity pathways at some point in the re-crystallization process.

### 1. Introduction

Titanite ( $CaTiSiO_5$ ) is a key accessory mineral for U-Pb geochronology and thermobarometry, yet it can exhibit complex compositional variability and petrogenetic behavior (see reviews by Frost et al., 2000; Kohn, 2017). Although this petrological complexity presents a challenge for interpreting U-Pb ages and P-T conditions derived from titanite analysis, it also presents an opportunity to evaluate the mineral reactions and grain-scale physico-chemical processes operating within titanite-bearing assemblages. The potential utility of titanite as a multi-

faceted petrological tool thus provides strong motivation for detailed investigation of the relationship among U-Pb isotopic systematics, trace element composition, and microstructural features preserved in metamorphic rocks.

One of the main obstacles to accurate titanite U-Pb geochronology is the propensity for titanite crystals to incorporate significant concentrations of common, or initial, Pb ( $Pb_0$ ) during growth, preventing acquisition of concordant U-Pb ratios. The abundance and composition of  $Pb_0$  can vary significantly in different crystallization environments, and may be variable between and within crystals from the same sample

\* Corresponding author at: School of Earth and Environmental Sciences, Queens College, City University of New York, 6530 Kissena Blvd., Flushing, NY 11367, USA.  
E-mail address: [jmarsh@qc.cuny.edu](mailto:jmarsh@qc.cuny.edu) (J.H. Marsh).

<http://dx.doi.org/10.1016/j.chemgeo.2017.06.029>

Received 16 September 2016; Received in revised form 20 June 2017; Accepted 22 June 2017  
0009-2541/ © 2017 Published by Elsevier B.V.

(e.g. Romer and Rötzler, 2003; Schoene and Bowring, 2006). The composition of Pb in local geochemical reservoirs may deviate significantly from model crustal Pb compositions (e.g. Stacey and Kramers, 1975), particularly when U and Th-rich precursor minerals are involved in titanite-forming reactions (Romer, 2001; Romer and Siegesmund, 2003). In these cases, application of the model  $Pb_0$  isotopic composition for correcting U-Pb data can lead to spurious results, and incorrect interpretation of the ages and apparent zoning patterns obtained.

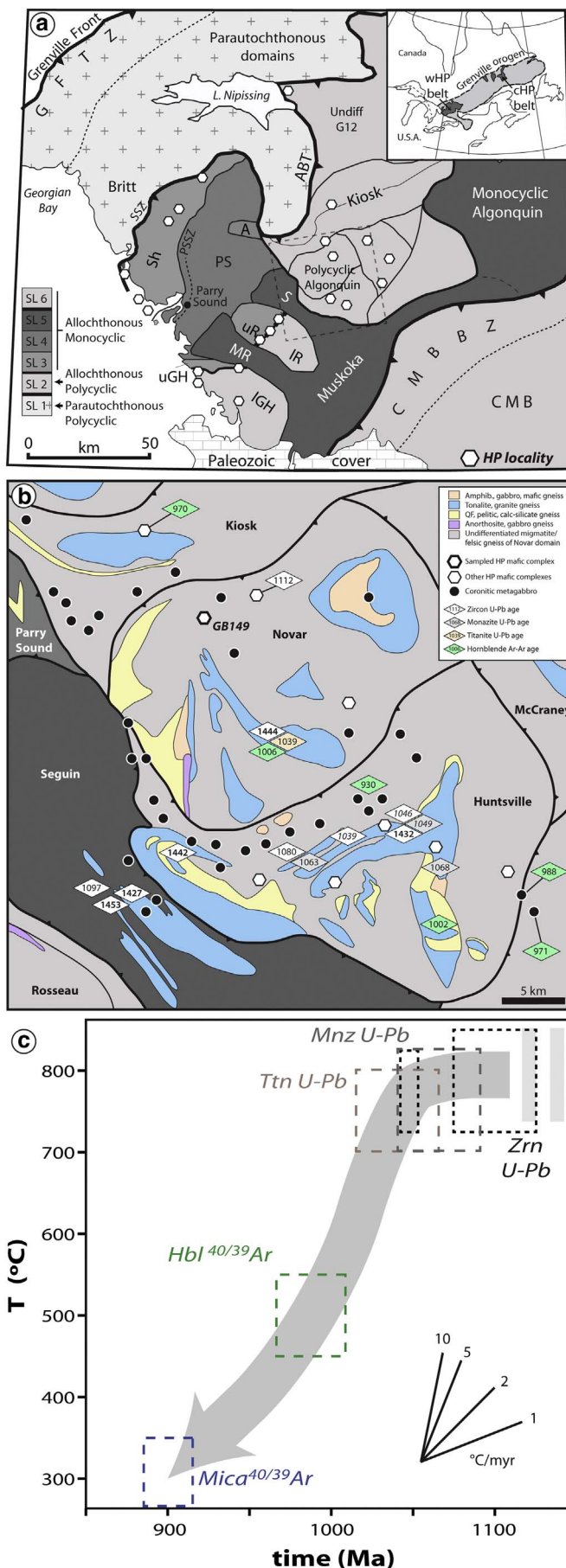
Interpretation of titanite U-Pb ages is further complicated by uncertainty over the temperature sensitivity of intracrystalline Pb diffusion. Early, field-based investigations using TIMS yielded titanite U-Pb ages from high grade metamorphic terranes that were younger than zircon and monazite U-Pb ages, consistent with closure to diffusive Pb-loss at temperatures  $\sim 600$ – $650$  °C (e.g. Heaman and Parrish, 1991; Mezger et al., 1991). Results from subsequent experimental studies supported higher closure temperatures ( $T_c$ ) of 650 °C and 750 °C for titanite crystals with 0.5 and 5 mm radii, respectively, for rocks cooling at  $\sim 5$  °C/Myr (Cherniak, 1993). Other studies found titanite to be more retentive, calculating U-Pb  $T_c$  of  $\sim 740$  °C for crystals as small as 0.3 mm (Schärer et al., 1994; Zhang and Schärer, 1996). More recently, a number of field-based studies utilizing in-situ U-Pb analyses of high-grade metamorphic titanite have shown that older metamorphic or protolith ages can be retained through extended residence ( $> 15$  Myr) at temperatures in excess of 750 °C, even for crystal sizes as small as 0.2 mm (Kohn and Corrie, 2011; Gao et al., 2012; Spencer et al., 2013). Based on these studies, Kohn (2017) suggested a nominal  $T_c$  of  $\sim 800$  °C for Pb in titanite, making it nearly as retentive as the high-T U-Pb geochronology stalwarts zircon and monazite.

The shift toward favoring a higher nominal  $T_c$  for diffusive Pb-loss in titanite has come with the recognition that younger U-Pb ages may record recrystallization processes that reset the trace element systems in metamorphic environments. Although a number of authors have attributed younger titanite U-Pb ages to recrystallization (e.g. Spencer et al., 2013; Bonamici et al., 2014, 2015; Stearns et al., 2016), the specific physico-chemical recrystallization process associated with the resetting is commonly not specified. Two main types of recrystallization processes are generally recognized for silicate minerals: (1) mechanically-induced recrystallization, where elemental components are mobilized by the movement of dislocations through the crystal lattice in response to externally-imposed differential stress (“dynamic recrystallization” e.g. Bonamici et al., 2014); and (2) dissolution-precipitation, where elemental components are exchanged as the crystal is dissolved and re-precipitated during changing equilibrium/saturation states with respect to an interstitial fluid/melt phase and associated minerals (see Putnis, 2009 for thorough discussion; Lucassen et al., 2011).

This contribution presents a detailed investigation of the U-Pb isotopic systematics and trace element composition for a suite of titanite crystals within a high pressure mafic granulite from the Canadian Grenville Province. Simultaneous acquisition of U-Pb isotope ratios and trace element abundances shows that (1) the  $Pb_0$  component is strongly radiogenic, (2) the  $Pb_0/Pb^*$  varies systematically from core to rim, as a function of both U and  $Pb_0$  concentration, and (3) variations in  $Pb_0$  concentration correlate with variations in specific minor/trace elements, potentially elucidating the crystal-chemical mechanisms behind incorporation of  $Pb_0$  and Pb diffusivity in titanite. Additionally, marginal increases in trace element concentration are shown to correspond with a range of distinctive textural features observed in backscattered electron (BSE) images, which are correlated with specific microstructural settings. These findings are discussed with reference to dissolution-precipitation, solid-state recrystallization, and thermally-activated volume diffusion.

## 2. Metamorphic and geochronological framework

The regional geological setting and petrogenetic relations associated



(caption on next page)

**Fig. 1.** (a) Lithotectonic domain map of western Central Gneiss Belt (CGB) within the Canadian Grenville Province. White dashed square shows area of panel b. Inset shows extent of Canadian Grenville Province and location of known high pressure belts. Western High Pressure (wHP) belt generally corresponds with area of CGB shown in panel a. See Marsh and Culshaw (2014) for abbreviations. (b) Simplified geological map of the Polycyclic Algonquin domain (modified after the Ontario Geological Survey, OGS Earth map), showing the distribution of the main metamorphic rock types, HP metabasites, and coronitic metagabbros. Studied samples from locality shown in bold polygon. Existing zircon, monazite, and titanite U-Pb ages, and hornblende Ar-Ar ages for Novar and Huntsville domains shown in colored rhombs (compiled from Cosca, 1989; Nadeau, 1990; Mezger et al., 1993; Nadeau and van Breemen, 1998; Marsh and Culshaw, 2014). Bold zircon ages represent protolith crystallization. Italic zircon and monazite ages from syn- to post-thrusting pegmatite dikes (Nadeau, 1990). (c) Temperature-time (T-t) diagram showing thermo-chronological constraints from above (Zrn U-Pb from coronitic metagabbros added (Davidson and van Breemen, 1988)), with T-t associated path for SL2 domains. Note early cooling of  $\geq 5$  °C/Ma between  $\sim 1050$ – $1000$  Ma, followed by cooling of  $\sim 2$  °C/Ma between  $1000$  and  $900$  Ma. (For interpretation of the references to color in this figure legend, the reader is referred to the web version of this article.)

with the titanite investigated here are described in detail by Marsh and Kelly (2017), and summarized here. The samples were collected from a decameter-scale metabasite complex (GB149) within the polycyclic,

allochthonous Novar subdomain of the Central Gneiss Belt (CGB), Grenville Province, Ontario (Fig. 1). Meter- to decameter-scale metabasite bodies are distributed throughout the allochthonous domains of the CGB, most of which have general characteristics of either coronitic metagabbros (coronites) or garnet and clinopyroxene-dominated eclogite/high-pressure (HP) granulite (see Rivers et al., 2002 for review). Coronites contain baddeleyite that yields U-Pb ages of ca. 1170 Ma, and is inferred to represent crystallization of the olivine-plagioclase gabbro protoliths (Davidson and van Breemen, 1988). Zircon rims surrounding baddeleyite generally yield U-Pb ages between 1046 and 1060 Ma, with a preferred  $^{207}\text{Pb}/^{206}\text{Pb}$  age of  $1047 \pm 5$  Ma inferred to represent the timing of granulite-facies metamorphism (Davidson and van Breemen, 1988). Eclogite/HP granulite-type metabasites, which do not exhibit coronitic textures, typically contain polydomainal zircon, with cores yielding ca. 1400 Ma (protolith) ages and rims yielding ca. 1090 Ma ages and REE patterns typical of HP metamorphism (Ketchum and Krogh, 1998; Marsh and Culshaw, 2014). This apparent difference in metamorphic age between coronites and eclogite/HP granulite metabasites has yet to be investigated systematically, but potentially reflects different reaction histories for each protolith type. Both types of

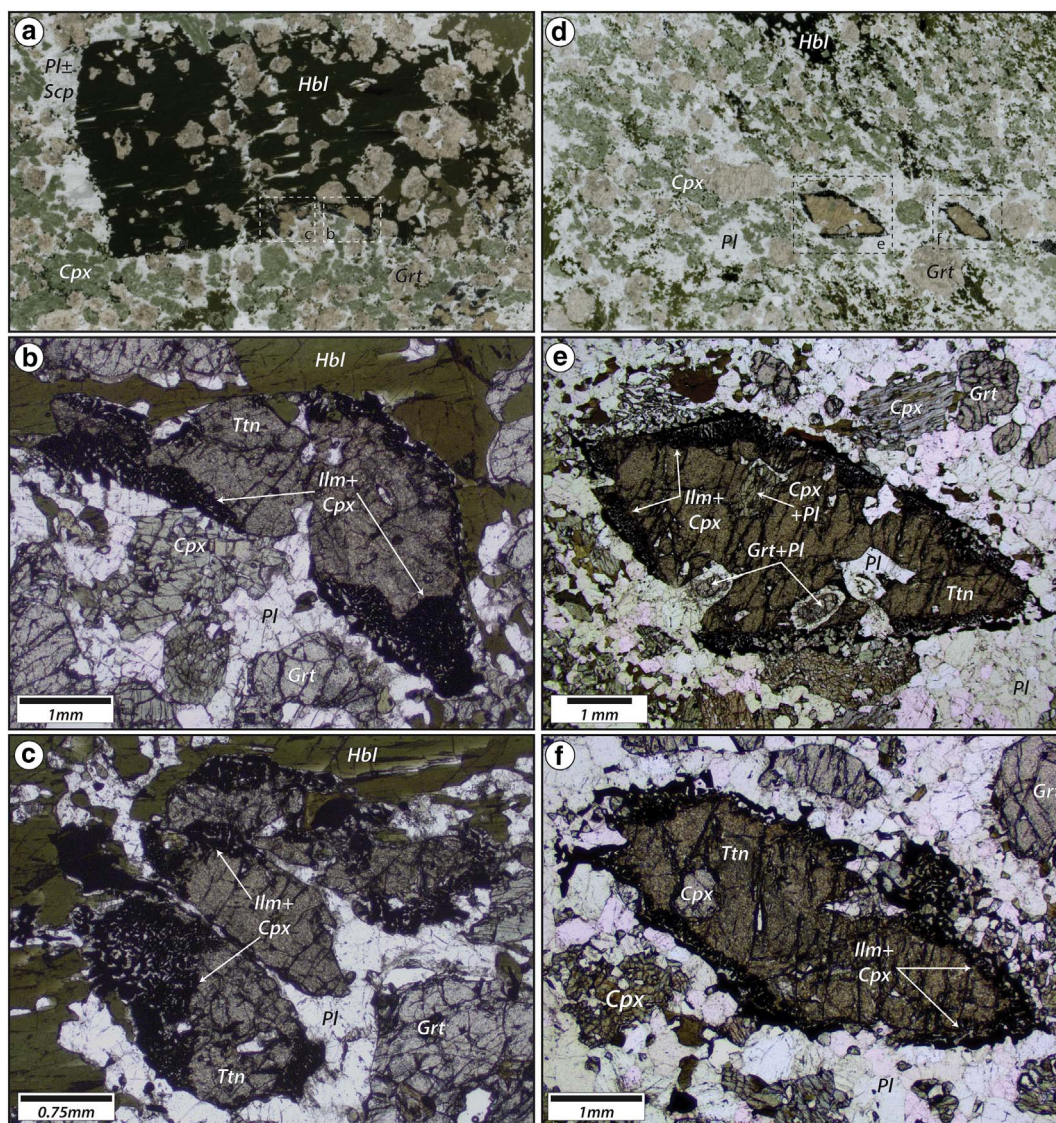


**Fig. 2.** Photomicrographs of studied samples. (a) GB149A microstructure containing hornblende megacryst within the garnet-clinopyroxene-plagioclase matrix and large titanite along the megacryst margin. Note dashed boxes showing locations of b & c. (b & c) Titanite crystals in boxed areas from a showing surrounding matrix phases and the characteristic clinopyroxene-ilmenite symplectite along the crystal margins. (d) GB149B microstructure containing large titanite within the garnet-clinopyroxene-plagioclase matrix. (e & f) Titanite crystals in boxed areas from d. Mineral abbreviations after Whitney & Evans, 2010.

metabasite typically have high-strain, lithologically mixed margins containing upper amphibolite-facies fabrics similar to those observed in the ca. 1020–1080 Ma felsic to intermediate orthogneisses that dominate the CGB (Davidson and van Breemen, 1988; Culshaw et al., 1997; Rivers et al., 2002; Marsh and Culshaw, 2014).

Within the southern Novar domain, Nadeau (1990) reported a  $1444 \pm 12$  Ma zircon U-Pb Discordia upper intercept age from the host orthogneiss (interpreted as the timing of igneous crystallization; Fig. 1b), with a highly-uncertain lower intercept of  $900 \pm 120$  Ma. A titanite U-Pb age of  $1039 \pm 2$  Ma was obtained from amphibolite near the dated orthogneiss, and interpreted by the authors to represent cooling through the  $\sim 650$  °C Pb closure temperature (Mezger et al., 1993). In the northern Novar domain, approximately 5 km ENE from GB149, Marsh and Culshaw (2014) obtained a zircon U-Pb age of  $1112 \pm 12$  Ma from a similar metabasite complex. Within the structurally overlying Huntsville domain (to the south of the Novar domain) “syn-thrusting” pegmatite dikes contain zircon yielding ages of  $1080 \pm 1$  Ma and  $1046 \pm 2$  Ma and monazite yielding ages of  $1063 \pm 5$  Ma and  $1049 \pm 2$  Ma, whereas zircon from a “post-thrusting” pegmatite dike yields an age of  $1039 \pm 4$  Ma (Nadeau, 1990). Hornblende  $^{40}\text{Ar}$ - $^{39}\text{Ar}$  ages throughout this part of the lower allochthonous domains typically fall between 970 and 1005 Ma, whereas biotite and muscovite  $^{40}\text{Ar}$ - $^{39}\text{Ar}$  ages cluster around ca. 900 Ma (Cosca, 1989). Compilation of these data indicate an extended period of high temperature ( $\sim 750$ – $800$  °C) metamorphism from  $\sim 1110$ – $1040$  Ma, followed by relatively slow cooling ( $\sim 5$  °C/Ma) to  $\sim 500$  °C by ca. 985 Ma and even slower cooling ( $\sim 2$  °C/Ma) to  $\sim 300$  °C by 900 Ma (Fig. 1c; Cosca, 1989).

Within the titanite-rich metabasite outcrop studied here, the primary mafic assemblage contains abundant leucosome, both interstitial to the garnet-clinopyroxene assemblage (Fig. 2) and as medium- to coarse-grained veins or pools locally forming interconnected networks. The leucosome veins have abundant cm-scale hornblende (*sensu lato*) megacrysts studded with abundant garnet inclusions, mm-scale titanite crystals, and locally abundant coarse-grained scapolite (Marsh and Kelly, 2017). Titanite crystals commonly contain abundant very fine- to medium-grained mineral inclusions resembling the matrix assemblage (Grt-Cpx-Hbl-Pl), and rarely contain small anhedral rutile inclusions. The titanite is partially to completely mantled by an ilmenite and clinopyroxene dominated symplectitic intergrowth, with abundant apatite and locally plagioclase and biotite (Fig. 2). X-ray mapping of the titanite crystals reveals systematic compositional zonation in Ti, Al, and F, with crystal interiors typically poorer in Ti and correspondingly richer in Al and F (Marsh and Kelly, 2017).

Marsh and Kelly (2017) proposed a clockwise P-T path with peak  $P = \sim 1.5$  GPa at  $T = \sim 750$  °C, followed by heating to supra-solidus conditions ( $> 800$  °C) and eventual cooling and decompression (Fig. S1). The calculated stability ranges of the Ti-rich phases indicate that titanite growth likely corresponded with resorption of clinozoisite and rutile into an increasingly Ca- and Ti-enriched anatectic melt near peak T conditions, with the clinopyroxene-ilmenite symplectite-forming during titanite breakdown reactions following melt crystallization during cooling to upper amphibolite facies conditions. Thus, the mineral associations and microtextural features apparently reflect these evolving P-T-X conditions and associated melting, grain- to outcrop-scale melt migration, and melt crystallization.

Detailed investigation of the titanite crystals using high-contrast backscattered electron (BSE) imaging exposed a number of intracrystalline features, each commonly associated with specific microstructural settings (Fig. 3). The main feature types include: (1) localized networks of irregularly-shaped polygonal subgrains up to a few ten of microns across, with bright boundaries  $\sim 1$ – $2$   $\mu\text{m}$  thick resembling recrystallization fronts (Fig. 3g, h). These subgrain networks are commonly observed where titanite is in contact with the plagioclase  $\pm$  K-feldspar matrix where no symplectite corona is present, as well as in some (but not all) areas that have been replaced by the symplectite; (2)

spaced, thin ( $< 1$   $\mu\text{m}$ ), curvilinear bands extending a short distance into the titanite perpendicular to the grain boundary. The bands are commonly spatially associated with the polygonal subgrains and symplectite coronas, and possibly represent micro-porosity pathways, healed microfractures, or other physico-chemical discontinuities (see Putnis, 2009 for extensive discussion); (3) thicker ( $< 5$   $\mu\text{m}$ ), bright bands parallel to the crystal boundary resembling marginal overgrowths (Fig. 3f, h). These bands are commonly observed where titanite is in contact with coarse hornblende or matrix clinopyroxene (Cpx<sub>2</sub> of Marsh and Kelly (2017)); (4) diffuse brightness gradients adjacent to subgrain boundaries, overgrowths, symplectite coronas, and locally along crystal margins in contact with the interstitial feldspar. The internal character of the gradients ranges from uniform to patchy or wispy, and their apparent width can be up to  $\sim 50$   $\mu\text{m}$  wide, although they are commonly  $< 25$   $\mu\text{m}$  or entirely absent in some locations (Fig. 3g–i). No clear correlation has been observed between brightness magnitude or gradient width and the width of associated subgrain boundary or corona, or the modal proportion of adjacent minerals within the coronas. Energy-dispersive X-ray analyses show REE enrichment associated with each of the bright features, including the diffuse gradients.

### 3. Zircon U-Pb geochronology and trace element composition

U-Pb geochronology and trace element analysis of GB149 zircon was conducted by LA-ICP-MS split-stream analyses in order to establish a chronological framework for the metamorphic evolution of the metabasite and the evaluation of titanite U-Pb systematics. Details on the analytical methods and processed U-Pb and trace element data are presented in the Supplementary materials (Tables S1 & S2).

Both of the samples analyzed from GB149 (one leucosome- and titanite-bearing and one leucosome- and titanite-free) yield nearly identical results, and were thus combined for the following discussion. Crystal interiors and rims each form distinctive populations on the Concordia diagram (Fig. S2a, b). Interior domains define a linear discordant array with upper intercept of  $1442 \pm 12$  Ma and a poorly-constrained lower intercept of  $336 \pm 240$  Ma. Rim domains are largely concordant, and define an upper intercept of  $1087 \pm 15$  Ma with a similarly poorly-constrained lower intercept of  $259 \pm 380$  Ma. A weighted average  $^{207}\text{Pb}/^{206}\text{Pb}$  age of  $1099 \pm 6$  Ma (MSWD = 1.02) was calculated from 45 of the 53 rim domain analyses, with eight analyses excluded due to extreme discordance or high uncertainty. The region of overlap between upper intercept and  $^{207}\text{Pb}/^{206}\text{Pb}$  weighted average, 1093–1102 Ma, is taken as the best estimate of the zircon rim age.

Zircon interior and rim domains also have distinctive trace element compositions (Fig. S2c–f). Interior domains typically have higher total REE (avg =  $323 \pm 206$  ppm (all trace element uncertainties are  $1\sigma$ )), stronger negative europium anomaly (avg  $\text{Eu}/\text{Eu}^* = 0.72 \pm 0.18$ ), and greater heavy REE enrichment (avg  $\text{Yb}_N/\text{Gd}_N = 53 \pm 29$ ), whereas rim domains typically have lower total REE (avg =  $55 \pm 71$  ppm), highly-variable but generally weaker negative europium anomaly (avg  $\text{Eu}/\text{Eu}^* = 0.84 \pm 0.28$ ), and smaller heavy REE enrichment (avg  $\text{Yb}_N/\text{Gd}_N = 13 \pm 12$ ). Th/U are typically much higher in interior domains (avg =  $0.68 \pm 0.19$ ) compared with rim domains (avg =  $0.13 \pm 0.17$ ), whereas Hf concentration are typically lower and more uniform in interior domains (avg =  $0.63 \pm 0.08$  wt%) compared with the more variably enriched rim domains (avg =  $0.97 \pm 0.17$  wt%). The trace element compositions of the interior domains are typical of zircon crystallized in intrusive igneous rocks (e.g. Hoskin and Schaltegger, 2003), and indicate that the  $1442 \pm 12$  Ma age represents the timing of protolith formation for this locality. Conversely, the low total REE and Th/U of rim domains is more typical of zircon formed during metamorphic (re)crystallization (e.g. Hoskin and Schaltegger, 2003; Rubatto et al., 2009; Marsh and Stockli, 2015), with the general lack of negative europium anomaly and

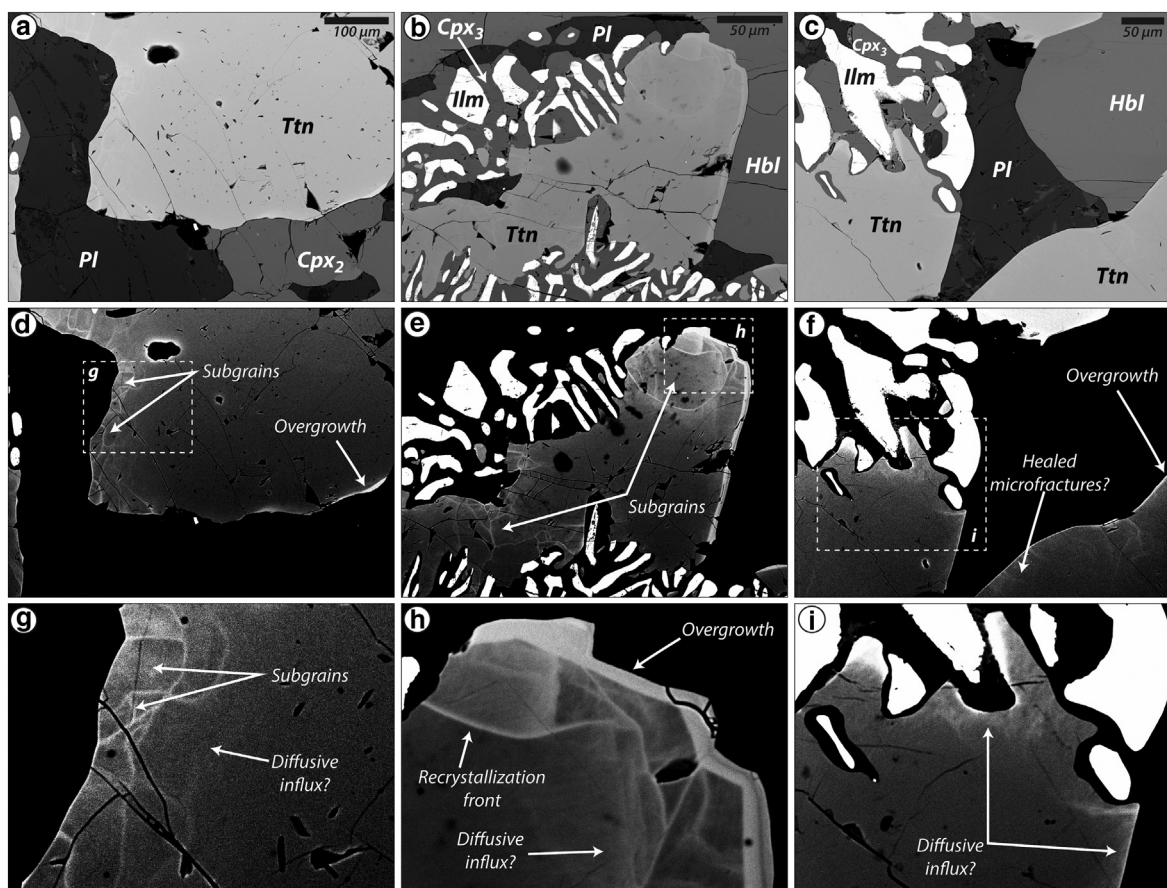


**Fig. 3.** Backscattered electron (BSE) images of titanite microstructures in GB149 samples. (a–c) “Normal”-contrast images showing titanite crystals in contact with coarse-grained hornblende, interstitial plagioclase, and clinopyroxene-ilmenite symplectite coronas. (d–i) High-contrast images showing various internal microstructures within titanite crystals defined by high brightness resulting from local trace element enrichment. Main features include: polygonal subgrains with bright boundaries (inferred recrystallization fronts) spatially associated with adjacent plagioclase, thin overgrowths spatially associated with adjacent clinopyroxene (Cpx<sub>2</sub>) and hornblende, spaced curved lines perpendicular to grain boundaries (inferred healed microfractures) spatially associated with adjacent plagioclase, and patchy to uniformly gradational zones (resembling diffusive influx).

low HREE enrichment suggesting that the 1093–1102 Ma rim domains (re)crystallized within a garnet-stable, plagioclase and/or melt-free (eclogite-type) assemblage (Rubatto, 2002; Rubatto and Hermann, 2007; Marsh and Culshaw, 2014).

#### 4. Titanite U-Pb geochronology and trace element composition

Titanite crystals were analyzed in-situ from polished thin sections cut from samples containing (1) a large, megacrystic hornblende within a non-foliated garnet-clinopyroxene assemblage (GB149A) and (2) a moderately foliated, hornblende-poor, garnet-clinopyroxene assemblage, with a higher proportion of leucosome (149B; Fig. 2). LA-ICP-MS split-stream analyses were completed along eight linear traverses across seven crystals (five from GB149A and two from GB149B). In order to evaluate the U-Pb and trace element systematics of the large titanite crystals, and potential intracrystalline U-Pb variability, the data were treated both in aggregate (i.e. combining all analyses within each sample) and within individual traverse segments (i.e. from crystal interior to margin). Details on the analytical methods and processed U-Pb and trace element data are presented in the Supplementary materials (Tables S3 & S4).

##### 4.1. General U-Pb and trace element systematics

Tera-Wasserburg diagrams of uncorrected U-Pb data for all spots in GB149A ( $n = 113$ ) and GB149B ( $n = 95$ ) yield linear discordant arrays characteristic of a cogenetic population with variable initial Pb/radiogenic Pb ratio ( $Pb_0/Pb^*$ ; Fig. 4a, b).  $^{207}Pb/^{206}Pb$  are comparatively low

in relation to  $^{238}U/^{206}Pb$ , with most spots closely approaching the Concordia, indicating that the contribution of  $Pb_0$  to the total Pb isotopic composition is low ( $^{206}Pb_0/^{206}Pb_T = 0.04–0.12$ ). Linear regression through the data indicate strongly radiogenic  $Pb_0$  values for both samples, with y-axis intercepts of  $0.503 \pm 0.045$  for GB149A and  $0.604 \pm 0.048$  for GB149B, providing data-defined initial  $^{207}Pb/^{206}Pb$  values ( $^{207}Pb_0/^{206}Pb_0$ ). Regression line lower intercepts yield U-Pb ages of  $1042 \pm 9$  Ma (MSWD = 1.2;  $2\sigma$  uncertainty) for GB149A and  $1052 \pm 8$  Ma (MSWD = 1.4) for GB149B, and a combined age for all GB149 analyses of  $1048 \pm 6$  Ma (MSWD = 1.4). Chondrite-normalized REE plots display relatively uniform MREE-enriched, HREE-poor trends for all crystals in both samples (Fig. 4c), with few spots from most crystals showing REE enrichment (see below).

##### 4.2. Intracrystalline U-Pb and trace element zoning

Within individual traverses, systematic intracrystalline spatial variability in titanite U-Pb composition becomes more apparent. U-Pb data from individual traverse segments define linear arrays in Tera-Wasserburg space; however, crystal interiors invariably have higher  $Pb_0/Pb^*$  compared to their adjacent crystal margins (Fig. 5). Higher  $Pb_0/Pb^*$  regions in the crystal interiors also have higher Al and lower Zr and REE, with lower Al and higher Zr and REE concentrations correlating with more nearly concordant U-Pb compositions (Fig. S3). Uncorrected U-Pb dates for individual spots in traverse profiles generally show systematic variation from core to rim, with old ( $\gg 1100$  Ma) dates in the crystal interiors and younger dates (ca. 1050–1090 Ma) along crystal margins (Figs. 6 & 7).  $^{207}Pb$ -corrected U-Pb spot dates calculated

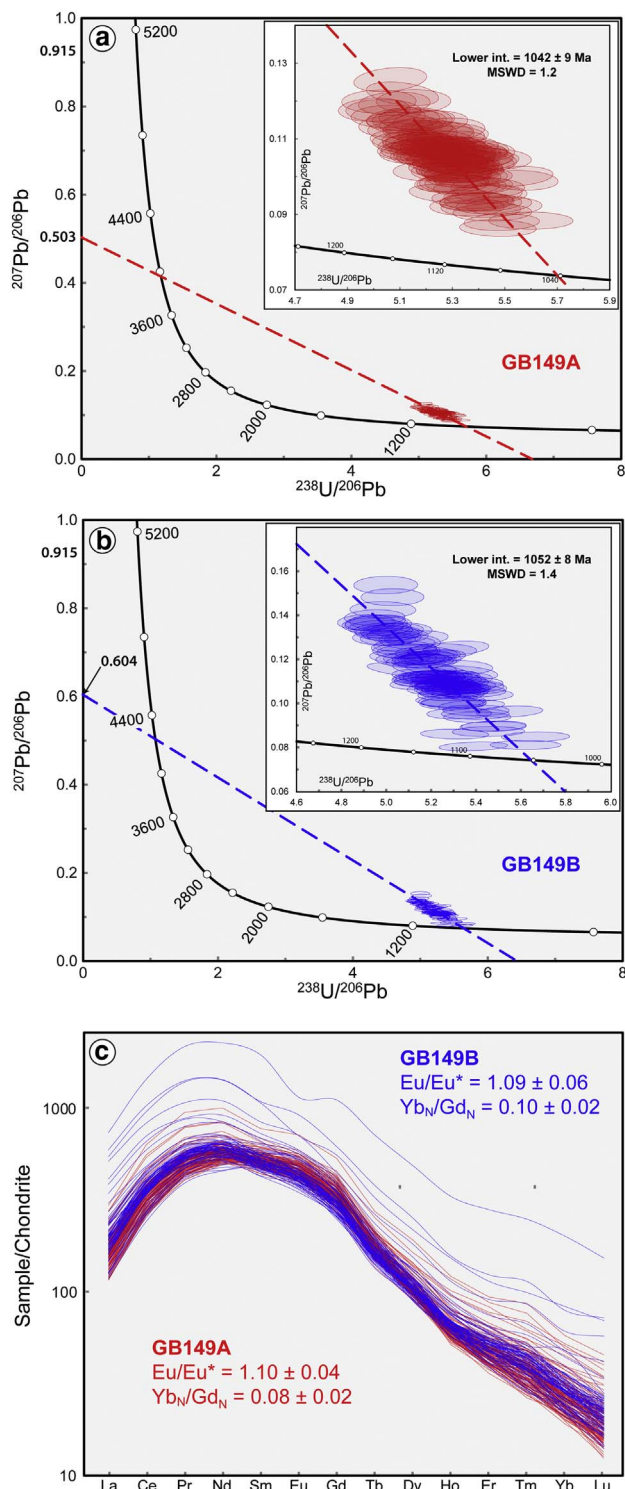


Fig. 4. (a & b) Tera-Wasserburg plots of uncorrected titanite U-Pb data for all spots in (a) GB149A ( $n = 113$ ) and (b) GB149B ( $n = 95$ ). Linear regression of the data defines Discordia with ordinate intercept (initial  $^{207}\text{Pb}/^{206}\text{Pb}$ ) of  $0.503 \pm 0.045$  for GB149A and  $0.604 \pm 0.048$  for GB149B. Discordia lower intercepts yield U-Pb dates of  $1042 \pm 9$  Ma for GB149A and  $1052 \pm 8$  Ma for GB149B. (c) Chondrite-normalized REE plot for GB149A (red) and GB149B (blue). (For interpretation of the references to color in this figure legend, the reader is referred to the web version of this article.)

using the regression intercept  $^{207}\text{Pb}_0/^{206}\text{Pb}_0$  value for each sample yield essentially unzoned profiles at dates between 1050 and 1020 Ma for crystals with lower  $^{207}\text{Pb}_0/^{206}\text{Pb}_0$  (e.g. 0.439 in T6.1; Fig. 6), whereas  $^{207}\text{Pb}$ -corrected U-Pb spot dates for crystals with higher  $^{207}\text{Pb}_0/^{206}\text{Pb}_0$  (e.g. 0.744 in T3.1; Fig. 7) have similarly shaped zonation patterns to

uncorrected profiles, but at dates 40–60 Myr younger (Fig. 7). Crystals with low regression  $^{207}\text{Pb}_0/^{206}\text{Pb}_0$  values show a clear correlation between the uncorrected U-Pb date, the calculated  $^{206}\text{Pb}_0/^{206}\text{Pb}_T$  (not shown), and the measured  $^{204}\text{Pb}/^{206}\text{Pb}$  and  $^{208}\text{Pb}/^{206}\text{Pb}$ , with higher values in the crystal centers and lower values along the margins.

For all crystals, the uncorrected U-Pb date profiles,  $^{206}\text{Pb}_0/^{206}\text{Pb}_T$ ,  $^{204}\text{Pb}/^{206}\text{Pb}$ , and  $^{208}\text{Pb}/^{206}\text{Pb}$  correspond closely with variations in Sr, and to a lesser degree, Al concentrations. Th/U varies significantly across the crystals, typically with the lowest values in the crystal interiors and gradational to step-like increases to maximum values within the crystal margins, whereas U is more uniformly low in crystal interiors with maximum values along the margins. In most crystals Th/U profiles closely correspond with Nb and P concentration profiles, and locally covary with  $^{208}\text{Pb}/^{206}\text{Pb}$  through portions of crystal interiors that typically contain the oldest uncorrected U-Pb dates. Neodymium and Zr profiles are nearly identical to U, and share broadly similar profile characteristics with Th/U, Nb, and P with lowest concentration in the crystal interiors.

Bivariate plots of  $^{206}\text{Pb}_0/^{206}\text{Pb}_T$  versus uncorrected  $^{206}\text{Pb}/^{238}\text{U}$  spot dates and selected trace element concentrations from GB149A further display the relationship between U-Pb systematics and composition (Fig. 8).  $^{206}\text{Pb}_0/^{206}\text{Pb}_T$  exhibit linear, positive correlations with uncorrected  $^{206}\text{Pb}/^{238}\text{U}$  dates, Al, and Sr, with crystal interiors typically having higher  $^{206}\text{Pb}_0/^{206}\text{Pb}_T$ , spot dates, Al, and Sr than the crystal margins. The regression line x-intercept for  $^{206}\text{Pb}_0/^{206}\text{Pb}_T$  versus uncorrected  $^{206}\text{Pb}/^{238}\text{U}$  spot dates (i.e.  $^{206}\text{Pb}_0/^{206}\text{Pb}_T = 0$ ) yields a value of 1039.6 Ma, nearly identical to the ages determined from regression of U-Pb isotopic data in Tera-Wasserburg space ( $1042 \pm 9$  Ma). Conversely, Nd, Zr, and U do not show a linear correlation with  $^{206}\text{Pb}_0/^{206}\text{Pb}_T$ . Each of these elements exhibit relatively uniform low concentrations within the crystal interiors, spanning much of  $^{206}\text{Pb}_0/^{206}\text{Pb}_T$  range (0.04–0.12), with higher concentrations in the crystal margins restricted to very low  $^{206}\text{Pb}_0/^{206}\text{Pb}_T$  (0.02–0.04).

#### 4.3. U-Pb and trace element characteristics of marginal microstructures

Viewing the marginal compositional variations within the context of the microstructural features, as observed in high-contrast BSE imaging, enables some clear associations to be established (Fig. 9). The bright recrystallization fronts associated with polygonal subgrains coincide with sharp, roughly two-fold increases in concentration of most heavy trace elements, including U, Th, REE, and HFSE. Within the subgrains, these trace element concentrations remain elevated proximal to the recrystallization fronts, but trend toward lower values similar to those within the crystal interiors over distances greater than  $\sim 25 \mu\text{m}$  (Fig. 9d, h). Diffuse brightness gradients associated with the symplectite coronas and marginal overgrowths also exhibit U, Th, REE, and HFSE enrichment; however, the concentrations increase gradually toward the crystal boundary commensurate with the brightness gradients and are of more variable magnitude (typically less than two-fold increases; Fig. 9h, l). In areas where both recrystallization fronts and diffuse gradients exist, the concentration profiles exhibit irregular shapes, apparently reflecting superimposition of the two processes (Fig. 9f–h).

## 5. Discussion

### 5.1. Timing of zircon and titanite growth

Field observations and micro-scale textural relations indicate that titanite crystallized within leucosome-rich zones interstitial and adjacent to a garnet and clinopyroxene-dominated assemblage (Marsh and Kelly, 2017). Phase equilibrium modeling for the metabasite bulk composition shows that titanite crystallization is possible at intermediate- to high-pressure granulite-facies conditions in regions of local Ca-enrichment, in this case associated with interactions with the calcic interstitial melt (Marsh and Kelly, 2017). Zircon rim domains from

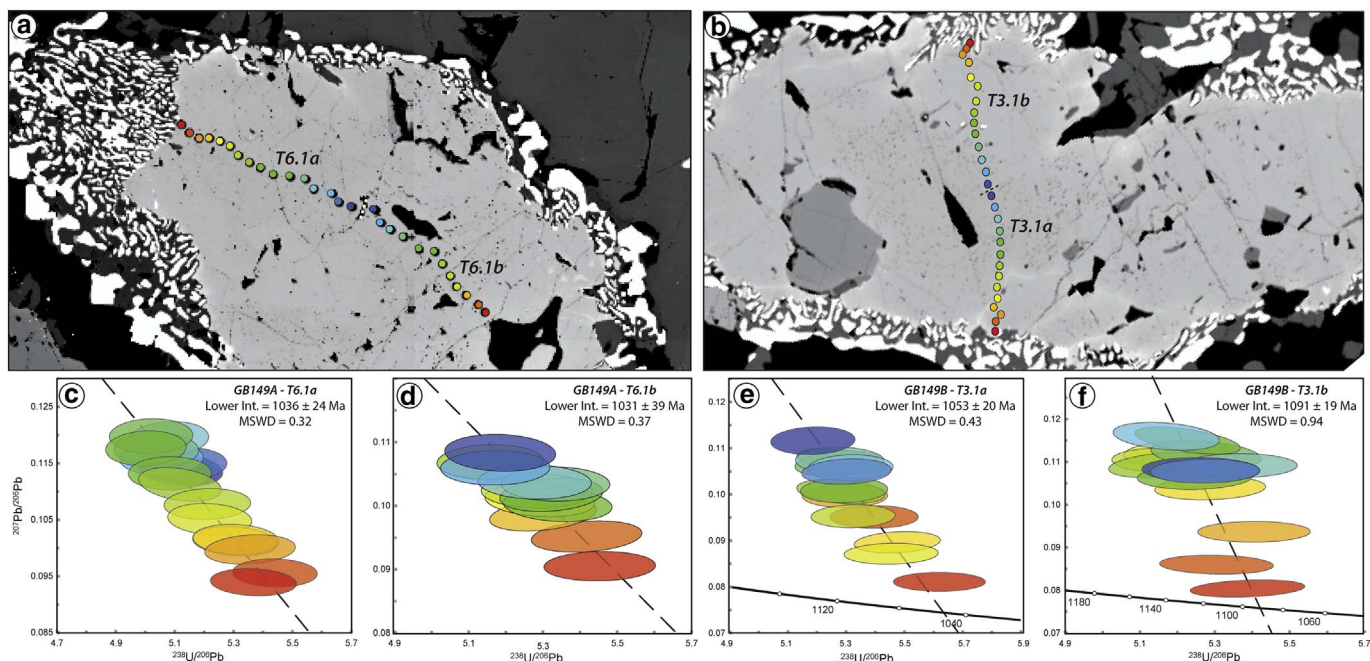


**Fig. 5.** Intracrystalline spatial variability in titanite U-Pb composition. (a) Backscattered electron (BSE) image showing LA-ICP-MS traverse 6.1 across titanite from GB149A (Fig. 2b). Spot colors correspond with data points shown in b–e. (b & c) Tera-Wasserburg diagrams for left and right half of traverse shown in A, color-coded for the spot locations. Note higher  $Pb_0/Pb^*$  in the grain interiors compared to the grain margins. (d) BSE image showing LA-ICP-MS traverse 3.1 across titanite from GB149B (Fig. 2f). (e & f) Tera-Wasserburg diagrams for lower and upper half of traverse shown in d.

these samples have trace element compositions consistent with growth or recrystallization in a garnet-stable, plagioclase and/or melt-poor assemblage, suggesting that the 1093–1102 Ma U-Pb age corresponds with the garnet-clinopyroxene-rutile assemblage that predates the titanite-producing, melt-present assemblage. This interpretation is strengthened by similar zircon ages and REE compositions determined for other leucosome-poor high-pressure metabasites in the CGB (Ketchum and Krogh, 1998; Marsh and Culshaw, 2014), the formation of which is presumably associated with an episode of relatively cold (< 750 °C) thickening prior to the regional high-temperature metamorphism associated with the “Ottawan” phase (ca. 1080–1030 Ma) of the Grenville orogeny (Culshaw et al., 1997; Rivers et al., 2002).

The low  $^{206}Pb_0/^{206}Pb_T$  of the investigated titanite indicates that the U-Pb isotopic composition is dominated by in-grown radiogenic Pb, and the lack of significant lateral dispersion in  $^{238}U/^{206}Pb$  suggests that Pb loss was minor relative to analytical precision, justifying an assumption of (near) concordance for the radiogenic portion of the U-Pb system. In light of these characteristics we interpret the  $1048 \pm 6$  Ma age from the unconstrained linear regression intercept to represent the age of titanite growth, indicating that high-pressure granulite-facies metamorphism (~825–850 °C) and leucosome crystallization occurred ~45 Myr after formation of the primary garnet-clinopyroxene eclogite assemblage. This timeframe is consistent with the  $1047 \pm 5$  Ma age of granulite-facies metamorphism inferred for the widely-distributed coronitic metagabbros (Davidson and van Breemen, 1988), as well as the 1046–1063 Ma zircon and monazite ages from syntectonic pegmatite within the superjacent Huntsville domain to the south (Nadeau, 1990).

## 5.2. Primary titanite growth

### 5.2.1. Compositional zoning and uptake

Systematic core to rim variation and correlation between U-Pb and trace element composition in GB149 titanite is apparent from Tera-Wasserburg topology and traverse profiles for each crystal. Trace element zoning is common in titanite crystallized in melt-present environments, typically with highest REE and HFSE concentrations in the cores and decreasing toward the rims (e.g. McLeod et al., 2011; Bruand

et al., 2014). However, high-contrast BSE images of GB149 titanite do not exhibit obvious zoning patterns through the crystal interiors, with essentially uniform U, Th, REE, and HFSE concentrations (near their minimum values). Conversely, elements such as Sr and Al do show decreasing core-rim concentrations in the crystal interiors that closely resemble the  $Pb_0$ -related zonation.

The spatial variation in  $^{206}Pb_0/^{206}Pb_T$ , indicates that titanite crystal interiors have higher  $Pb_0/Pb^*$  than outer portions. To some degree this variation reflects the higher U concentrations along the crystal margins (> 100 ppm); however, the decreasing  $^{206}Pb_0/^{206}Pb_T$  (from their maximum values) within the uniformly low U crystal interiors (Figs. 6–8) suggests progressively decreasing  $Pb_0$  uptake during growth. The strong positive correlation between  $^{206}Pb_0/^{206}Pb_T$  and uncorrected  $^{206}Pb/^{238}U$  dates is consistent with the interpretation that intracrystalline U-Pb age zonation reflects mixing of  $Pb^*$  with spatially variable concentrations of  $Pb_0$  (Fig. 8), as opposed to diffusional Pb-loss from the crystal margins. This inference is strengthened by the positive correlation between  $^{206}Pb_0/^{206}Pb_T$  and Sr concentrations, as discussed below. The magnitude of  $Pb_0$  uptake during growth could potentially have been controlled by some combination of the following factors: (1) temporal variations in the breakdown of proximal Pb-bearing precursor minerals, (2) slow Pb diffusivity in the matrix relative to titanite growth rate (i.e. Rayleigh distillation), or (3) changing partitioning of Pb between titanite and an evolving interstitial melt. Experimentally-determined partition coefficients between titanite and dacitic melt suggest that trace element uptake should be strongly influenced by the major element composition of the melt (Prowatke and Klemme, 2005). However, for most melt compositions investigated Pb should partition more readily into titanite ( $D_{Ttn/melt} = 0.87$ ) than U ( $D_{Ttn/melt} = 0.14$ ) and Th ( $D_{Ttn/melt} = 0.28$ ), suggesting that differential titanite-melt trace element partitioning played an important role in controlling the composition of crystal interiors (Fig. 10).

The positive correlation between  $Pb_0$  and Sr across the entire range of concentrations suggests a similar substitution mechanism into the sevenfold Ca-site (Frost et al., 2000), which is consistent with the nearly identical ionic radii and isovalence of Sr and  $Pb^{2+}$ . The weaker positive correlation between  $Pb_0$  and Al indicates that substitutions involving Al

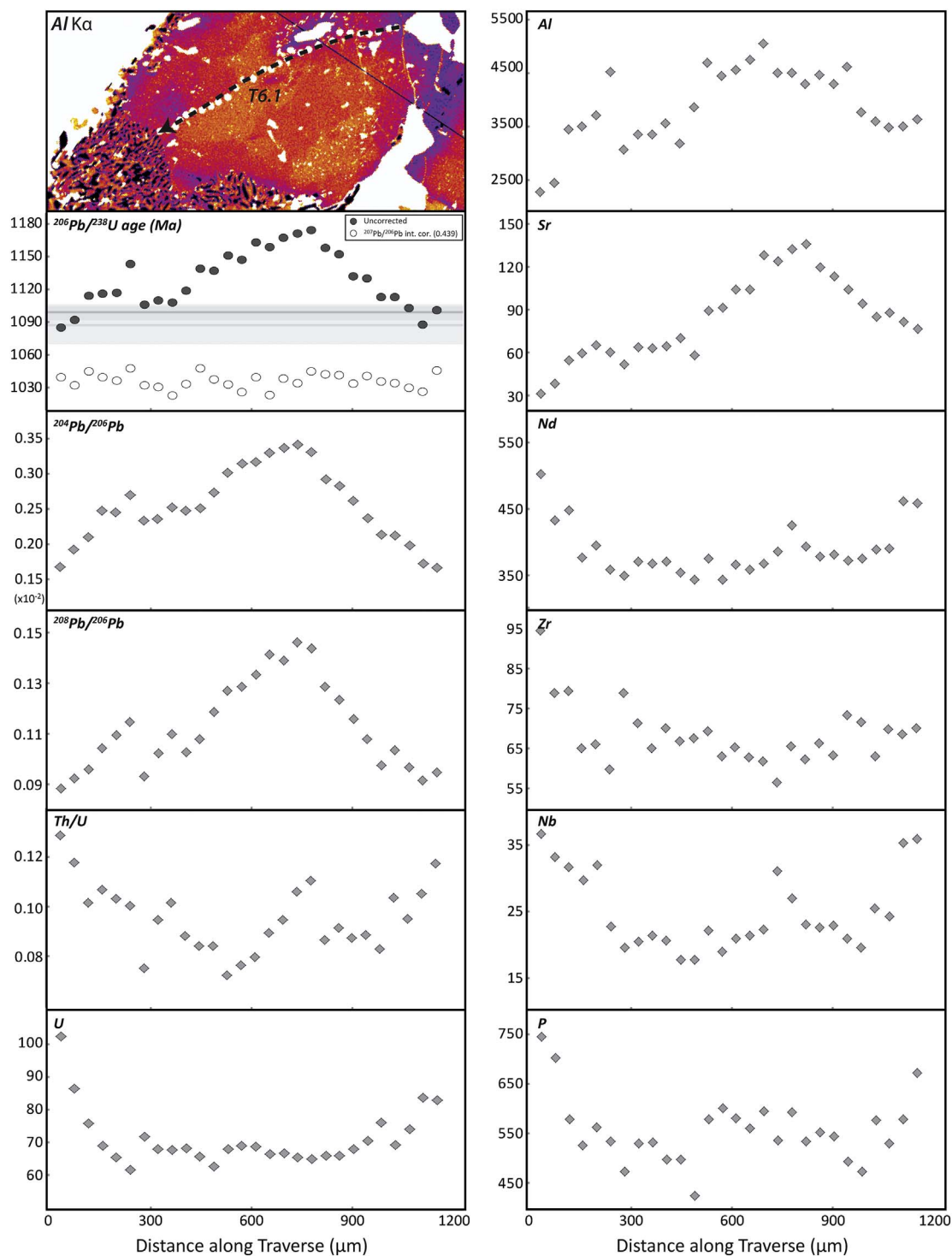


**Fig. 6.** U-Th-Pb and selected trace element composition across GB149A titanite traverse 6.1, shown on aluminum (Al) map in upper left panel. Uncorrected  $^{206}\text{Pb}/^{238}\text{U}$  dates are shown in dark gray, and  $^{207}\text{Pb}$ -corrected dates calculated using the linear regression upper intercept are shown in white ( $^{207}\text{Pb}/^{206}\text{Pb} = 0.439$ ). Horizontal gray bands represent zircon rim Discordia intercept ( $1087 \pm 15$  Ma) and  $^{207}\text{Pb}/^{206}\text{Pb}$  weighted average ( $1099 \pm 6$  Ma) ages with  $2\sigma$  uncertainty. Measured  $^{204}\text{Pb}/^{206}\text{Pb}$ ,  $^{208}\text{Pb}/^{206}\text{Pb}$ , Th/U ratios, and U, Al, Sr, Nd, Zr, Nb, and P concentrations are shown for the same transect.

in the octahedral (Ti) site varied similarly to those controlling Pb uptake. Crystal-chemical factors associated with increased Al concentration in titanite would tend to disfavor the incorporation of Sr, suggesting that local availability or fluid/mineral buffering may be more likely to influence relationships between Al and Sr (and Pb) uptake (e.g. Lucassen et al., 2011). The uniformly low concentrations of U, Th, REE and HFSE across crystal interiors do not correlate with the systematic  $\text{Pb}_0$ , Sr, or Al zoning, indicating that uptake of these elements was not

coupled during titanite growth.

### 5.2.2. Potential initial Pb sources

The low average  $^{207}\text{Pb}_0/^{206}\text{Pb}_0$  value ( $0.561 \pm 0.034$ ) defined by linear regression of all analyses indicates that the  $\text{Pb}_0$  incorporated into titanite during growth was highly radiogenic compared with the 0.916 value predicted by the Stacey and Kramers (1975) Pb-evolution model for 1050 Ma. However, inspection of the  $^{207}\text{Pb}_0/^{206}\text{Pb}_0$  value calculated

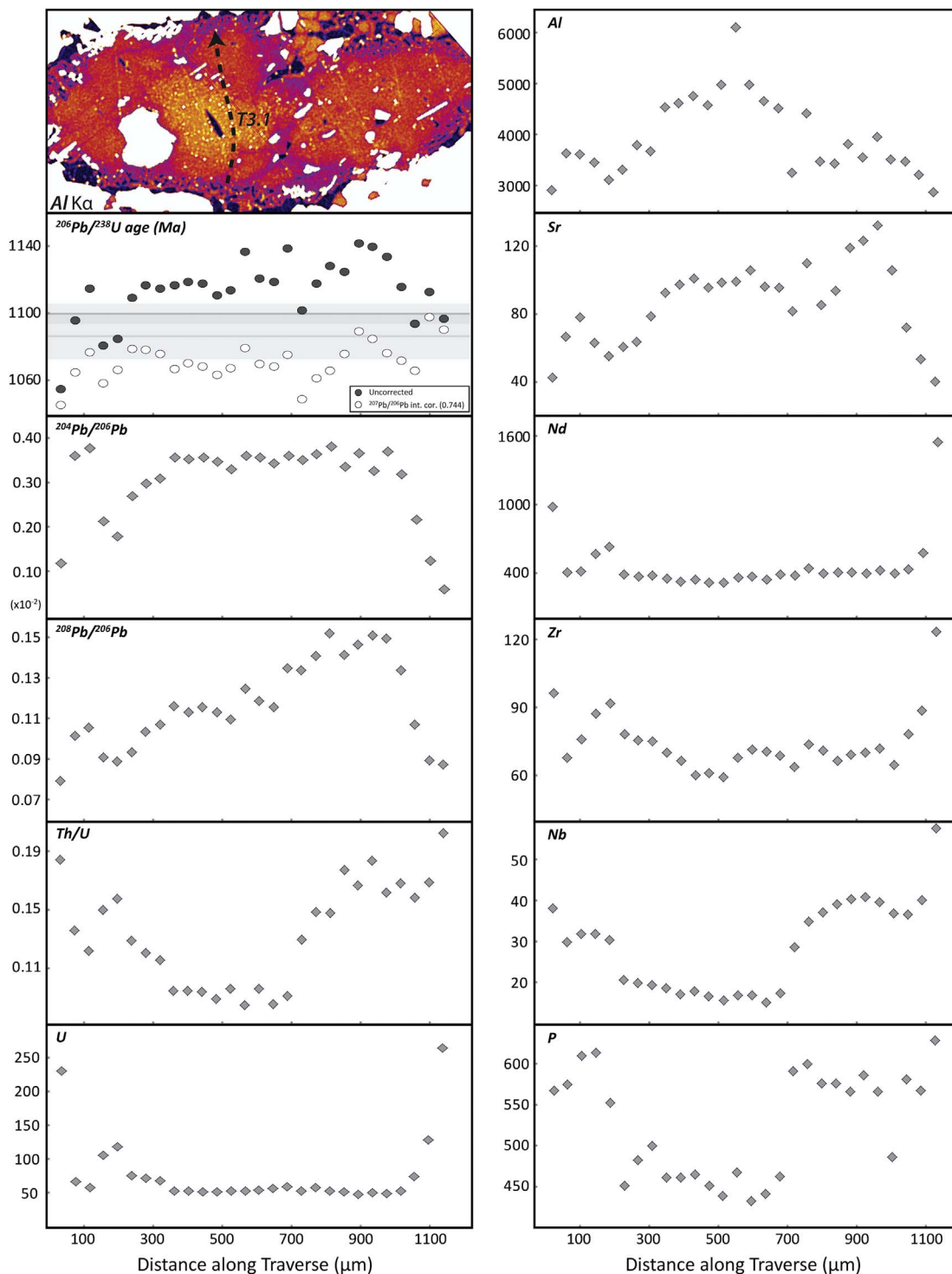


**Fig. 7.** U-Th-Pb and selected trace element composition across GB149B titanite traverse 3.1, shown on aluminum (Al) map in upper left panel. Uncorrected  $^{206}\text{Pb}/^{238}\text{U}$  dates are shown in dark gray, and  $^{207}\text{Pb}$ -corrected dates calculated using the linear regression upper intercept are shown in white ( $^{207}\text{Pb}/^{206}\text{Pb} = 0.744$ ). Horizontal gray bands represent zircon rim Discordia intercept ( $1087 \pm 15$  Ma) and  $^{207}\text{Pb}/^{206}\text{Pb}$  weighted average ( $1099 \pm 6$  Ma) ages with  $2\sigma$  uncertainty. Measured  $^{204}\text{Pb}/^{206}\text{Pb}$ ,  $^{208}\text{Pb}/^{206}\text{Pb}$ , Th/U ratios, and U, Al, Sr, Nd, Zr, Nb, and P concentrations are shown for the same transect.

for individual crystals, which ranges from 0.439 to 0.744, demonstrates that the  $\text{Pb}_0$  composition was variable within the volumes captured in the two thin sections. Radiogenic Pb isotopic compositions are typically associated with growth from a local geochemical reservoir influenced by the breakdown of U- or Th-rich precursor minerals, from which significant  $\text{Pb}^*$  was released (Romer, 2001; Romer and Siegesmund, 2003). Quantitative petrological models and field based-studies have shown that high-temperature (metaluminous to peralkaline) crustal

melts are likely to have heterogeneous and strongly radiogenic Pb compositions, due to a higher degree of melting and assimilation of accessory minerals (e.g. Hogan and Sinha, 1991; Waight and Leshner, 2010). Thus, the leucosome found throughout the GB149 outcrop appears to have been isotopically-heterogeneous, likely resulting from spatially variable dissolution of U- and Th-bearing minerals into the melt prior to titanite crystallization.

Although U and Th are both incompatible, their partitioning into

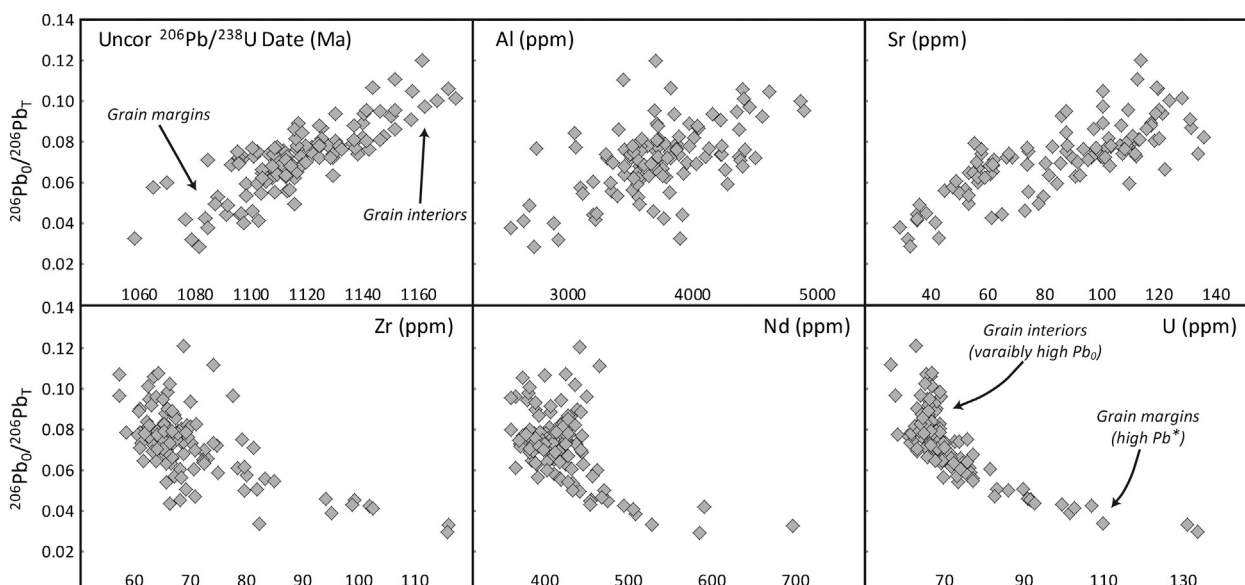


**Fig. 8.** Plots showing  $^{206}\text{Pb}_0/^{206}\text{Pb}_T$  versus uncorrected  $^{206}\text{Pb}/^{238}\text{U}$  spot dates and trace element composition for GB149A.  $^{206}\text{Pb}/^{238}\text{U}$  spot dates, Al and Sr show positive correlations with U-Pb dates, with x-intercept ( $^{206}\text{Pb}_0/^{206}\text{Pb}_T = 0$ ) of 1039.6 Ma falling close to the pooled age determined from Tera-Wasserburg regression lower intercept ( $1042 \pm 9$  Ma). Nd, Zr, and U concentrations do not correlate with U-Pb dates in grain interiors, exhibiting essentially uniformly low concentrations, with high concentration along the margins trending toward younger uncorrected  $^{206}\text{Pb}/^{238}\text{U}$  spot dates.

titanite relative to a silicate melt or fluid should be roughly equal (or moderately Th-favored; e.g. Tiepolo et al., 2002; Prowatke and Klemme, 2005), suggesting the low Th/U in the GB149 titanite interiors ( $< 0.2$ ) results from growth in a Th-depleted, U-enriched environment. Radiogenic Pb-producing minerals common in crustal rocks include the low Th/U minerals rutile and zircon, and variable to high Th/U minerals allanite, apatite, monazite, and xenotime. Petrographic analysis from GB149 shows abundant rutile and clinzoisite, and minor zircon included in garnet porphyroblasts, and abundant zircon in the matrix. The lack of rutile and clinzoisite in the matrix indicates that these eclogite-facies minerals must have been consumed in the interstitial melt prior to or during the titanite-producing reactions, and thus likely contributed to U-Th-Pb systematics of the reservoir (Fig. 10). Small ( $\sim < 20 \mu\text{m}$ ) anhedral rutile are observed within titanite in a few locations, indicating direct replacement and U-Th-Pb inheritance from the precursor rutile by titanite in some locations. Clinzoisite consumption in the titanite-forming reactions also may be represented by the high Sr and Al concentrations in the crystal interiors. Among the higher Th/U minerals, breakdown of the phosphates apatite, monazite, and xenotime would likely generate local enrichment of slow-diffusing P at the reaction site. X-ray maps and spot traverses do show distinct areas of P enrichment within the titanite, and a good correlation exists between Th/U and P (Figs. 6 & 7). Thus, the dissolution of a phosphate mineral into the melt likely contributed to the U-Th-Pb systematics of titanite interiors as well.

### 5.3. Modification by post-crystallization processes

The clear spatial association between U, Th, REE, and Zr enrichment and distinctive microstructural features observed along titanite margins indicates that the composition of the crystals were locally modified after initial growth. As with most minerals, titanite is susceptible to a number of common physico-chemical processes in magmatic and metamorphic environments, including: (1) solid-state “dynamic” recrystallization or crystal-plastic deformation in response to differential stresses (Spencer et al., 2013; Bonamici et al., 2014), (2) dissolution and regrowth (precipitation) within an intergranular fluid or melt as conditions controlling its solubility evolve with time (e.g. Lucassen et al., 2011, 2012; McLeod et al., 2011), and (3) intracrystalline diffusion of ions that are mobile at the ambient environmental conditions (Mezger

et al., 1991; Cherniak, 1993, 2006; Watson and Cherniak, 2015). The degree to which each of these processes may have been active in the investigated samples is evaluated below.

#### 5.3.1. Recrystallization/dissolution-precipitation

The bright bands that define the edges of polygonal subgrains within titanite from both samples appear to record a recrystallization process, with the trace element enriched bands possibly representing the inboard edge of a migrating subgrain (i.e. recrystallization fronts). Although titanite crystals in GB149B are aligned with their long axis parallel to the weakly developed foliation, GB149A exhibits no discernible foliation and titanite are clustered with no preferred orientation. Furthermore, none of the investigated titanite exhibit petrographic evidence for crystal-plastic deformation (i.e. no sweeping extinction or deformation-related microstructures), and EBSD maps show  $< 5^\circ$  lattice misorientation within the analyzed crystals and no spatial association between lattice misorientation and most of the observed subgrains. Thus, it appears more likely that a chemically-driven recrystallization or dissolution-precipitation process is responsible for the observed subgrains and associated marginal compositional variations.

The clear microstructural association of the investigated subgrains with adjacent matrix feldspar (plagioclase with minor K-feldspar), suggests that their formation is related to interaction with the interstitial melt, presumably late in the crystallization process. Subgrains are also found adjacent to the clinopyroxene-ilmenite symplectite coronas in some areas; however, the observation of subgrains in areas lacking coronas, and the absence of subgrains in titanite adjacent to coronas in some areas, indicates that the subgrains are not genetically related to the symplectite-forming reaction.

In magmatic and fluid-rich environments, titanite dissolution and re-precipitation is common (e.g. Lucassen et al., 2011; McLeod et al., 2011; Bruand et al., 2014). Changes in temperature, pressure, or melt/fluid compositions may destabilize titanite and lead to dissolution, with subsequent system evolution enabling regrowth as titanite again becomes saturated with respect to the interstitial melt/fluid (Putnis, 2009). In this model for subgrain formation, the high trace element concentrations along the recrystallization fronts could have resulted from local trace element enrichment of the adjacent melt/fluid (i.e. released from the dissolved titanite), followed by trace element uptake

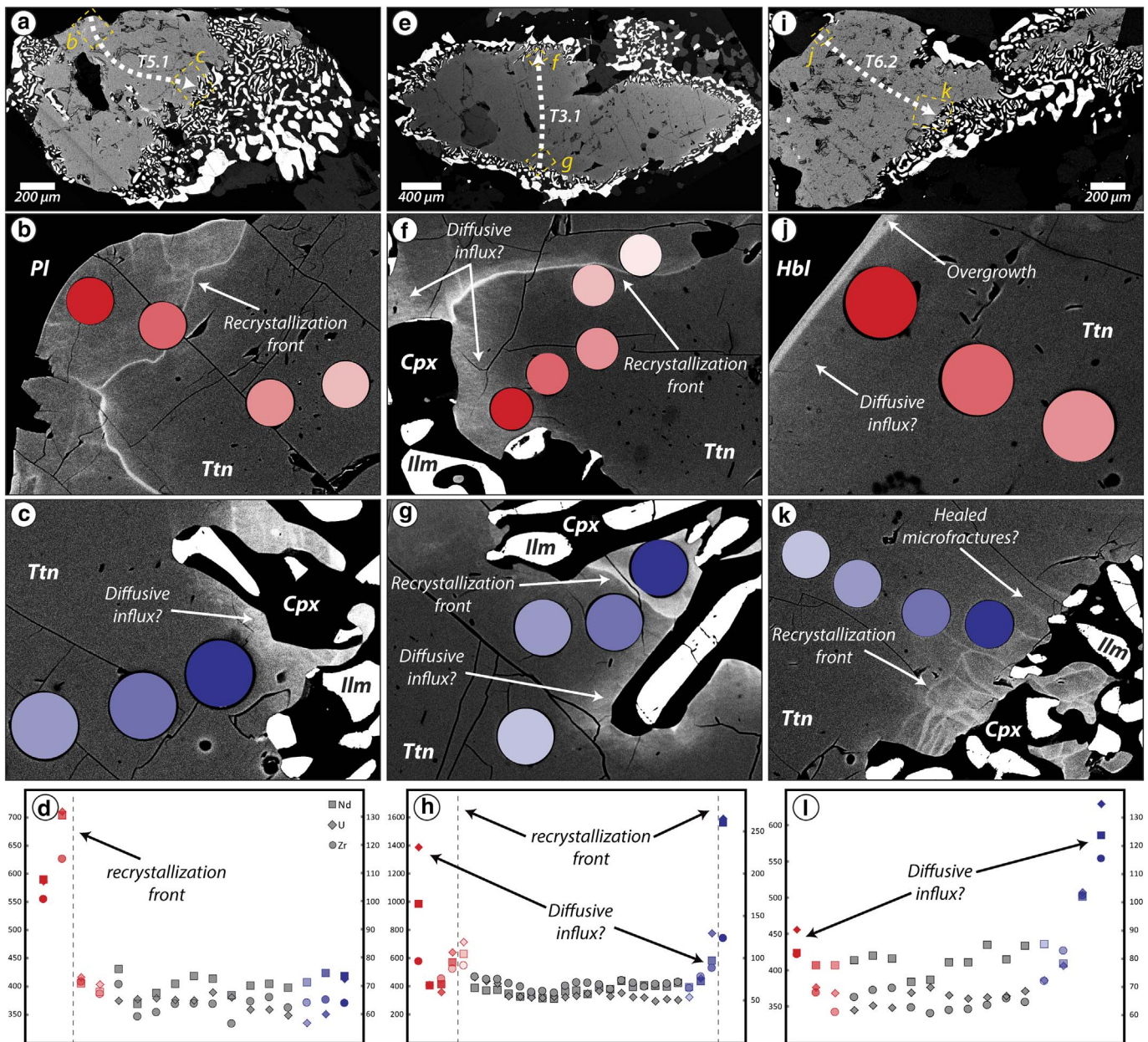


Fig. 9. Relationship between marginal microstructures and trace element composition in GB149 titanite. (a, e, i) BSE images showing locations of high-magnification images shown below. Note yellow dashed box and figure label. (b–c, f–g, j–k) High-contrast BSE images showing locations of LA-ICP-MS spot analyses in bottom panels. Note color-coded shading of spots and data points. (d, h, l) Trace element concentrations across LA-ICP-MS traverses show in top panels, with color-coded data points correlating with spots show in above panels. Nd shown on left axis, Zr and U shown on right axis. (For interpretation of the references to color in this figure legend, the reader is referred to the web version of this article.)

into titanite during regrowth. This model is consistent with the high equilibrium titanite/melt partition coefficients for REE and HFSE (e.g. Tiepolo et al., 2002; Prowatke and Klemme, 2005). However, the high concentrations of the incompatible U and Th as well as REE and HFSE, and the return of all trace element concentrations to lower values within the subgrain interiors, suggests that uptake was largely driven by local enrichment along a thin boundary layer and may not have followed equilibrium partitioning.

The thin (bright) titanite overgrowths observed adjacent to large hornblende crystals are also suggestive of precipitation from a locally-trace element-enriched melt/fluid. Experimental studies of REE and Zr partitioning between hornblende and dacitic melt are roughly an order of magnitude less than for titanite and dacitic melt (Sisson, 1994). Subsolidus titanite-hornblende REE and Zr partitioning determined from retrogressed eclogite yield similar titanite-favored partitioning coefficients (Sassi et al., 2000). Although no data on the partitioning of

U and Th is available from this study, titanite would be expected to incorporate U and Th from a late crystallizing melt/fluid over the adjacent hornblende.

### 5.3.2. Intracrystalline diffusion

Although the data presented here lack the spatial resolution and precision (for U-Pb data) required to quantitatively evaluate elemental diffusivity, the general compositional correlations and profile shapes, and U-Pb isotope systematics, enable qualitative assessment of element mobility within the titanite crystals during high-temperature residence.

**5.3.2.1. Pb diffusion.** The lack of resolvable dispersion in uncorrected  $^{206}\text{Pb}/^{238}\text{U}$  values in Tera-Wasserburg space and absence of near-rim decreases in  $^{207}\text{Pb}_0$ -corrected dates suggests that Fickian-type Pb-loss was not significant. Furthermore,  $^{204}\text{Pb}/^{206}\text{Pb}$  and  $^{206}\text{Pb}_0/^{206}\text{Pb}_T$  have nearly identical profiles to Sr - an element with roughly four orders of

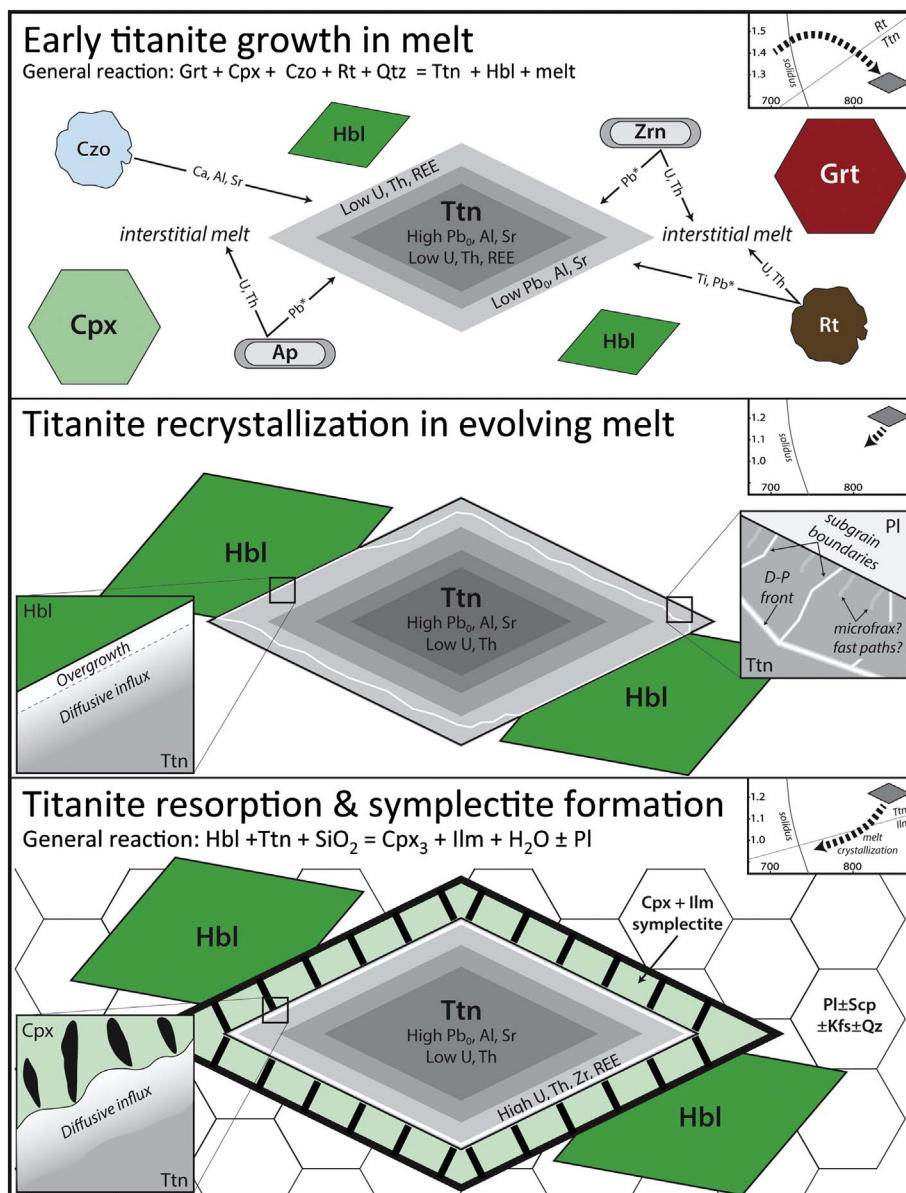


**Fig. 10.** Conceptual model for trace element uptake and modification in titanite. Upper panel shows initial titanite growth in anatectic melt near peak T conditions (inset P-T diagram), with clinzoisite, rutile, and U-Pb accessory minerals (e.g. apatite and zircon) partially dissolved into the melt. Middle panel shows titanite recrystallization/dissolution-precipitation associated with varying solubility in an evolving melt. Lower panel shows titanite resorption associated with clinopyroxene-ilmenite symplectite formation during cooling and decompression (see inset) where melt has mostly crystallized to form the  $Pl \pm Scp \pm Kfs \pm Qz$  leucocratic matrix. In middle and lower panels, white lines and shading represent high trace element concentrations associated with the depicted processes. P-T paths in inset based on the petrogenetic evolution of the GB149 samples from Marsh and Kelly (2017).

magnitude slower diffusivity than Pb in the experiments of Cherniak (1993, 1995) - consistent with Sr and Pb having experienced similar length scales of diffusion in these samples. Based on the published Pb diffusion parameters (Cherniak, 1993), complete re-equilibration of the titanite U-Pb system is predicted over length scales of hundreds of micrometers for rocks cooling from 800 °C at a rate of  $\leq 10$  °C/Myr (Watson and Cherniak, 2015). The titanite studied here mostly have radii of  $< 0.5$  mm and crystallized at temperatures in excess of 800 °C, with the thermal peak followed by slow cooling ( $\sim 5$  °C/Myr) through the hornblende  $^{40}Ar/^{39}Ar$  closure temperature ( $\sim 500$  °C; Cosca, 1989)  $\sim 50$ – $80$  Myr later (Fig. 1c). Our results support slow Pb diffusivity in titanite, even at high temperature conditions, as has been proposed in a number of recent studies (Kohn, 2017 and references therein). The specific mechanisms controlling Pb diffusivity are not elucidated from this study; however, we speculate that limitations on the rate of Pb diffusion may result from complex coupled substitutions, potentially involving the slower diffusing Sr and/or REE in the seven-fold Ca site.

**5.3.2.2. U, REE, and Zr diffusion.** The diffuse brightness gradients associated with the symplectite coronas and marginal overgrowths exhibit U, Th, REE, and HFSE enrichments similar to the thin

recrystallization fronts, but have profile shapes similar to those generated by Fickian-type diffusion (Fig. 9). Variable magnitudes and length scales of trace element enrichment and the absence of correlations with corona widths or modal proportion of adjacent minerals, suggests that diffusive influx was heterogeneous and potentially complicated by additional physico-chemical processes.

Based on experimental data of Cherniak (1995, 2006), the  $\sim 25$   $\mu m$  average length scale of apparent diffusive trace element influx is compatible with linear cooling from 800 to 700 °C (i.e. avg.  $T = 750$  °C) over  $\sim 1$  Myr for Zr and  $\sim 24$  Myr for Nd in oxidizing conditions (annealed in air). However, Nd diffusion at the reduced conditions that tend to favor the clinopyroxene-ilmenite symplectite forming reaction (e.g. Xirouchakis and Lindsley, 1998; Harlov et al., 2006) is implausibly slow, reaching 25  $\mu m$  length scales in  $\sim 2$  Byrs. Alternatively, the titanite consuming, symplectite-forming, reaction may not have been driven by changing  $fO_2$ , but instead by decreased  $a_{H_2O}$  or changing P-T conditions (Frost et al., 2000; Xirouchakis et al., 2001), leaving Nd diffusion over tens of micrometers over 25 Myr timeframes as a possibility. Although there is no published data estimating U diffusivity in titanite, based on experimentally-derived values for apatite and zircon (Cherniak, 2010) U is expected to be essentially

immobile with regards to volume diffusion, even at unreasonably long high-temperature residence.

One factor that may have enhanced the diffusive influx adjacent to the symplectite coronas (i.e. enabling diffusive-like profiles for U), is the inward-moving titanite boundary. As the titanite-consuming reaction proceeds, the liberation of trace elements should produce high concentrations along the boundary, with almost all trace elements of interest having a higher affinity for titanite than the product phases (with the exception of HFSE potentially having an equal or higher affinity for ilmenite). This should set up steep concentration gradients, providing a large potential for driving inward diffusion. Another possibility to consider is that the diffusive transport of the trace elements may have been enhanced by fast diffusion pathways generated during the recrystallization process (Putnis, 2009). The melt/fluid-present dissolution-precipitation process that appears to have affected the titanite crystals may have generated micro-porosity within the newly precipitated material near the reaction front (Putnis, 2009). Thus subgrains formed during earlier dissolution-precipitation reactions may have higher permeability enabling enhanced chemical transport from the crystal boundary, as has been observed in experiments of titanite replacing rutile in the presence of aqueous fluids (e.g. Lucassen et al., 2012), possibly resulting in the wispy bright bands observed within many of the diffuse gradients. Microfracturing of the reactant ahead of the symplectite-forming reaction front may have also occurred, now represented by the short, bright lines extending into the titanite from the crystal boundary (Fig. 9k). This process has been shown to be associated with pseudomorphic replacement by minerals of differing molar volume, and provides fast transport pathways for chemical transport and localized reactions (Janssen et al., 2008; Putnis, 2009).

Supplementary data to this article can be found online at <http://dx.doi.org/10.1016/j.chemgeo.2017.06.029>.

## Acknowledgements

This work was supported by the Research Foundation of CUNY. AJS acknowledges support from Penn State. Danny & Lisa Stockli provided analytical assistance with LA-ICP-MS analyses at the University of Texas. Andrew Kylander-Clark provided analytical assistance at UCSB and helpful discussion of titanite U-Pb data reduction approaches. Cindy Lin, of Townsend-Harris High School, assisted with early petrographic characterization of the studied samples. Chloe Bonamici and an anonymous reviewer provided helpful reviews, and Klaus Mezger is thanked for his editorial handling.

## References

- Bonamici, C.E., Kozdon, R., Ushikubo, T., Valley, J.W., 2014. Intragrain oxygen isotope zoning in titanite by SIMS: cooling rates and fluid infiltration along the Carthage-Colton Mylonite Zone, Adirondack Mountains, NY, USA. *J. Metamorph. Geol.* 32, 71–92.
- Bonamici, C.E., Fanning, C.M., Kozdon, R., Fournelle, J.H., Valley, J.W., 2015. Combined oxygen-isotope and U-Pb zoning studies of titanite: new criteria for age preservation. *Chem. Geol.* 398, 70–84.
- Bruand, E., Storey, C., Fowler, M., 2014. Accessory mineral chemistry of high Ba-Sr granites from northern Scotland: constraints on petrogenesis and records of whole-rock signature. *J. Petrol.* 55, 1619–1651.
- Cherniak, D.J., 1993. Lead diffusion in titanite and preliminary results on the effects of radiation damage on Pb transport. *Chem. Geol.* 110, 177–194.
- Cherniak, D.J., 1995. Sr and Nd diffusion in titanite. *Chem. Geol.* 125, 219–232.
- Cherniak, D.J., 2006. Zr diffusion in titanite. *Contrib. Mineral. Petrol.* 152, 639–647.
- Cherniak, D.J., 2010. Diffusion in accessory minerals: zircon, titanite, apatite, monazite and xenotime. In: Zhang, Y., Cherniak, D.J. (Eds.), *Diffusion in Minerals and Melts. Reviews in Mineralogy and Geochemistry* 72. Mineralogical Society of America, pp. 827–869.
- Cosca, M.A., 1989. Cooling and Inferred Uplift/Erosion History of the Grenville Orogen, Ontario: Constraints From  $^{40}\text{Ar}/^{39}\text{Ar}$  Thermochronology. (PhD dissertation) University of Michigan (223 p).
- Culshaw, N.G., Jamieson, R.A., Ketchum, J.W.F., Wodicka, N., Corrigan, D., Reynolds, P.H., 1997. Transect across the northwestern Grenville orogen, Georgian Bay, Ontario: polystage convergence and extension in the lower orogenic crust. *Tectonics* 16, 966–982.
- Davidson, A., van Breemen, O., 1988. Baddeleyite–zircon relationships in coronitic metagabbro, Grenville Province: implications for geochronology. *Contrib. Mineral. Petrol.* 100, 291–299.
- Frost, B., Chamberlain, K., Schumacher, J., 2000. Sphene (titanite): phase relations and role as a geochronometer. *Chem. Geol.* 172, 131–148.
- Gao, X.Y., Zheng, Y.F., Chen, Y.X., Guo, J., 2012. Geochemical and U–Pb age constraints on the occurrence of polygenetic titanites in UHP metagranite in the Dabie orogen. *Lithos* 136, 93–108.
- Harlov, D., Tropper, P., Seifert, W., Nijland, T., Forster, H.J., 2006. Formation of Al-rich titanite ( $\text{CaTiSiO}_4\text{O}-\text{CaAlSiO}_4\text{OH}$ ) reaction rims on ilmenite in metamorphic rocks as a function of  $\text{fH}_2\text{O}$  and  $\text{fO}_2$ . *Lithos* 88, 72–84.
- Heaman, L., Parrish, R., 1991. U–Pb geochronology of accessory minerals. In: Heaman, L., Ludden, J.N. (Eds.), *Applications of radiogenic isotope systems to problems in geology. Short Course Handbook*. 19. Mineral Assoc Canada, Toronto, Canada, pp. 59–102.
- Hogan, J.P., Sinha, A.K., 1991. The effect of accessory minerals on the redistribution of lead isotopes during crustal anatexis: a model. *Geochim. Cosmochim. Acta* 55, 335–348.
- Hoskin, P.W.O., Schaltegger, U., 2003. The composition of zircon and igneous and metamorphic petrogenesis. In: Hanchar, J.M., Hoskin, P.W.O. (Eds.), *Zircon. Rev. in Mineral. and Geochem* 53. pp. 27–62.
- Janssen, A., Putnis, A., Geisler, T., Putnis, C.V., 2008. The mechanism of experimental oxidation and leaching of ilmenite in acid solution. In: *Proc. Ninth International Congress for Applied Mineralogy*, pp. 503–506.
- Ketchum, J.W.F., Krogh, T.E., 1998. U–Pb constraints on high-pressure metamorphism in the southwestern Grenville orogen. In: *Goldschmidt Conference Abstracts*. 62A. pp. 775–776.
- Kohn, M.J., 2017. Titanite petrochronology. In: Kohn, M.J., Engi, M., Lanari, P. (Eds.), *Petrochronology: Methods and Applications. Reviews in Mineralogy and Geochemistry* 83. Mineralogical Society of America, pp. 419–441.
- Kohn, M.J., Corrie, S.L., 2011. Preserved Zr-temperatures and U–Pb ages in high-grade metamorphic titanite: evidence for a static hot channel in the Himalayan orogen. *Earth Planet. Sci. Lett.* 311, 136–143.
- Lucassen, F., Franz, G., Dulski, P., Romer, R.L., Rhede, D., 2011. Element and Sr isotope signatures of titanite as indicator of variable fluid composition in hydrated eclogite. *Lithos* 121, 12–24.
- Lucassen, F., Franz, G., Wirth, R., Weise, M., Hertwig, A., 2012. The morphology of the reaction front of the dissolution-precipitation reaction rutile + wollastonite = titanite in time series experiments at 600 °C/400 MPa. *Am. Mineral.* 97, 828–839.
- Marsh, J.H., Culshaw, N., 2014. Timing and conditions of high-pressure metamorphism in the western Grenville Province: constraints from accessory mineral composition and phase equilibrium modeling. *Lithos* 201, 402–417.
- Marsh, J.H., Kelly, E.D., 2017. Petrogenetic relations among titanium-rich minerals in an anatectic high-pressure granulite. *J. Metamorph. Geol.* <http://dx.doi.org/10.1111/jmg.12252>.
- Marsh, J.H., Stockli, D.F., 2015. Zircon U–Pb and trace element zoning characteristics in an anatectic granulite domain: insights from LASS-ICP-MS depth profiling. *Lithos* 239, 170–185.
- McLeod, G.W., Dempster, T.J., Faithfull, J.W., 2011. Deciphering magma-mixing processes using zoned titanite from the Ross of Mull Granite, Scotland. *J. Petrol.* 52, 55–82.
- Mezger, K., Rawnsley, C., Bohlen, S., Hanson, G., 1991. U–Pb garnet, sphene, monazite, and rutile ages: implications for the duration of high-grade metamorphism and cooling histories, Adirondack Mts., New York. *J. Geol.* 99, 415–428.
- Mezger, K., Essene, E.J., van der Pluijm, B.A., Halliday, A.N., 1993. U–Pb geochronology of the Grenville Orogen of Ontario and New York: constraints on ancient crustal tectonics. *Contrib. Mineral. Petrol.* 114, 13–26.
- Nadeau, L., 1990. Tectonic, Thermal and Magmatic Evolution of the Central Gneiss Belt, Huntsville Region Southwestern Grenville Orogen. (PhD dissertation) Carleton University (269 p).
- Nadeau, L., van Breemen, O., 1998. Plutonic ages and tectonic setting of the Algonquin and Muskoka allochthons, Central Gneiss Belt, Grenville Province, Ontario. *Can. J. Earth Sci.* 35, 1423–1438.
- O’Brein, P.J., Rötzler, J., 2003. High-pressure granulites: formation, recovery of peak conditions and implications for tectonics. *J. Metam. Geol.* 21, 3–20.
- Prowatke, S., Klemme, S., 2005. Effect of melt composition on the partitioning of trace elements between titanite and silicate melt. *Geochim. Cosmochim. Acta* 69, 695–709.
- Putnis, A., 2009. Mineral replacement reactions. In: Oelkers, E.H., Schott, J. (Eds.), *Thermodynamics and Kinetics of Water-Rock Interaction. Reviews in Mineralogy and Geochemistry* 70. Mineralogical Society of America, pp. 87–124.
- Rivers, T., Ketchum, J., Indares, A., Hynes, A., 2002. The high pressure belt in the Grenville Province: architecture, timing, and exhumation. *Can. J. Earth Sci.* 39, 867–893.
- Romer, R.L., 2001. Lead incorporation during crystal growth and the misinterpretation of geochronological data from low- $^{238}\text{U}/^{204}\text{Pb}$  metamorphic minerals. *Terra Nova* 13, 258–263.
- Romer, R.L., Rötzler, J., 2003. Effect of metamorphic reaction history on the U–Pb dating of titanite. In: Vance, D., Müller, W., Villa, I.M. (Eds.), *Geochronology: Linking the Isotopic Record With Petrology and Textures*. Geological Society, London, Special Publication 220. pp. 147–158.
- Romer, R.L., Siegesmund, S., 2003. Why allanite may swindle about its true age. *Contrib. Mineral. Petrol.* 146, 297–307.
- Rubatto, D., 2002. Zircon trace element geochemistry: distribution coefficients and the link between U–Pb ages and metamorphism. *Chem. Geol.* 184, 123–138.
- Rubatto, D., Hermann, J., 2007. Experimental zircon/melt and zircon/garnet trace element partitioning and implications for the geochronology of crustal rocks. *Chem.*

- Geol. 241, 38–61.
- Rubatto, D., Hermann, J., Berger, A., Engi, M., 2009. Protracted fluid-induced melting during Barrovian metamorphism in the Central Alps. *Contrib. Mineral. Petrol.* 158, 703–722.
- Sassi, R., Harte, B., Carswell, D.A., Yujing, H., 2000. Trace element distribution in Central Dabie eclogites. *Contrib. Mineral. Petrol.* 139, 298–315.
- Schärer, U., Zhang, L.S., Tapponnier, P., 1994. Duration of strike-slip movements in large shear zones: the Red River belt China. *Earth Planet. Sci. Lett.* 126, 379–397.
- Schoene, B., Bowring, S.A., 2006. U–Pb systematics of the McClure Mountain syenite: thermochronological constraints on the age of the  $^{40}\text{Ar}/^{39}\text{Ar}$  standard MMhb. *Contrib. Mineral. Petrol.* 151, 615–630.
- Sisson, T.W., 1994. Hornblende-melt trace-element partitioning measured by ion microprobe. *Chem. Geol.* 117, 331–344.
- Spencer, K.J., Hacker, B.R., Kylander-Clark, A.R.C., Andersen, T.B., Cottle, J.M., Stearns, M.A., Poletti, J.E., Seward, G.G.E., 2013. Campaign-style titanite U–Pb dating by laser ablation ICP: implications for crustal flow, phase transformations and titanite closure. *Chem. Geol.* 341, 84–101.
- Stacey, J.S., Kramers, J.D., 1975. Approximation of terrestrial lead isotope evolution by a two-stage model. *Earth Planet. Sci. Lett.* 26, 207–221.
- Stearns, M.A., Cottle, J.M., Hacker, B.R., Kylander-Clark, A.R.C., 2016. Extracting thermal histories from the near-rim zoning in titanite using coupled U–Pb and trace-element depth profiles by single-shot laser-ablation split stream (SS-LASS) ICP-MS. *Chem. Geol.* 422, 13–24.
- Tiepolo, M., Oberti, R., Vannucci, R., 2002. Trace-element incorporation in titanite: constraints from experimentally determined solid/liquid partition coefficients. *Chem. Geol.* 191, 105–119.
- Waight, T.E., Leshner, C.E., 2010. Pb isotopes during crustal melting and magma mingling — a cautionary tale from the Miki Fjord macrodike, central east Greenland. *Lithos* 118, 191–201.
- Watson, E.B., Cherniak, D.J., 2015. Quantitative cooling histories from stranded diffusion profiles. *Contrib. Mineral. Petrol.* 169, 57.
- Whitney, D.L., Evans, B.W., 2010. Abbreviations for names of rock-forming minerals. *Am. Mineral.* 95, 185–187.
- Xirouchakis, D., Lindsley, D.H., 1998. Equilibria among titanite, hedenbergite, fayalite, quartz, ilmenite, and magnetite: experiments and internally consistent thermodynamic data for titanite. *Am. Mineral.* 83, 712–725.
- Xirouchakis, D., Lindsley, D.H., Xirouchakis, D., Lindsley, D.H., Frost, B.R., 2001. Assemblages with titanite (CaTiO<sub>5</sub>SiO<sub>4</sub>), Ca–Mg–Fe olivine and pyroxenes, Fe–Mg–Ti oxides, and quartz: part II. application. *Am. Mineral.* 86, 254–264.
- Zhang, L.S., Schärer, U., 1996. Inherited Pb components in magmatic titanite and their consequence for the interpretation of U–Pb ages. *Earth Planet. Sci. Lett.* 138, 1–4.
- Zheng, Y.F., Hermann, J., 2014. Geochemistry of continental subduction-zone fluids. *Earth Planets Space* 66, 93–109.